Amino Acid-Induced Interface Charge Engineering Enables Highly Reversible Zn Anode

*Haotian Lu[#], Xuanlin Zhang[#], Minghe Luo, Keshuang Cao, Yunhao Lu, Ben Bin Xu, Hongge Pan, Kai Tao and Yinzhu Jiang**

Haotian Lu, Xuanlin Zhang, Minghe Luo, Keshuang Cao, Prof. Yinzhu Jiang
School of Materials Science and Engineering, State Key Laboratory of Clean Energy Utilization, ZJU-Hangzhou Global Scientific and Technological Innovation Centre, Zhejiang University, Hangzhou 310027, China
E-mail: yzjiang@zju.edu.cn

Prof. Yunhao Lu
Zhejiang Province Key Laboratory of Quantum Technology and Device, Department of Physics, Zhejiang University, Hangzhou 310027, China

Prof. Ben Bin Xu
Mechanical and Construction Engineering, Faculty of Engineering and Environment, Northumbria University, Newcastle upon Tyne NE1 8ST, UK

Prof. Hongge Pan
Institute of Science and Technology for New Energy, Xi'an Technological University, Xi'an 710021 China

Prof. Kai Tao
State Key Laboratory of Fluid Power and Mechatronic Systems & Key Laboratory of Advanced Manufacturing Engineering of Zhejiang Province, School of Mechanical Engineering, Zhejiang University, Hangzhou 310027, China

[#]H.L. and X.Z. contributed equally to this work.

Keywords: aqueous rechargeable zinc battery; zinc anode; amino acid additive; cycling stability; interface charge engineering

Abstract: Despite impressive merits of low-cost and high-safety electrochemical energy storage for aqueous zinc ion batteries, researchers struggled long against unsolved issues of dendrite growth and side reactions of zinc metal anode. Herein, a new strategy of zinc-electrolyte interface charge engineering induced by amino acid additive is demonstrated for highly reversible zinc plating/stripping. Through electrostatic preferential absorption of positively charged arginine molecules on the surface of zinc metal anode, a self-adaptive zinc-electrolyte interface is established for the inhibition of water adsorption/hydrogen evolution and the guidance of uniform zinc deposition. Consequently, an ultra-long stable cycling up to 2200 hours at a high current density of 5 mA cm^{-2} is achieved under an areal capacity of 4 mAh cm^{-2}. Even cycled at an ultra-high current density of 10 mA cm^{-2}, 900 hours-long stable cycling

is still demonstrated, indicating a reliable self-adaptive feature of zinc-electrolyte interface. This work provides a new perspective of interface charge engineering in realizing highly reversible bulk zinc anode that could prompt its practical application in aqueous rechargeable zinc batteries.

1. Introduction

Rechargeable lithium-ion batteries (LIBs) have made huge commercial success ranging from portable electronics, electric vehicles to grid-scale energy storage. [1-4] However, the long-existing concerns regarding the intrinsic safety hazards and the limited lithium resources which shadow the development of LIBs from the very beginning, have dramatically steered the development of non-lithium safe batteries. [5-10] Aqueous zinc ion batteries (AZIBs), one of the non-lithium safe batteries, has attracted considerable attention due to the natural abundance of zinc, the intrinsic safety of aqueous electrolyte and the low redox potential/high theoretic capacity of zinc anode toward high energy batteries. [11-14] The research on AZIB is currently undergoing the phase transition from the usage of conventional alkaline electrolyte to the neutral/mildly acidic one, which is hypothesised to be corrosion free from the strong alkaline to yield stable zinc plating/stripping processes. [15-18] Unfortunately, recent studies have proved above hypothesis to be another fantasy since corrosion reaction and zinc dendrite growth still occur in the neutral/mildly acidic electrolyte, [19] which are caused by the hydrogen evolution reaction (HER), the formation of electrochemically inactive by-products (such as $ZnSO_4[Zn(OH)_2]_3$ (ZSH) in $ZnSO_4$ electrolyte) and the uneven deposition of zinc. [20-22] These problems will unavoidably lead to the accelerated decay of Zn anode, cause poor reversibility of zinc plating/stripping, and degrade life span of the whole battery system.

To date, there have been various strategies proposed in improving the reversibility of bulk Zn anode, including constructing artificial functional layer, [23-29] introducing electrolyte additives, [30-34] and employing highly concentrated electrolytes. [35] The artificial layers, mostly composed of polymers or inorganic materials, can block the contact between the electrolyte and anode, guide the uniform distribution of Zn^{2+}, and thus exhibit improved cycle life and Coulombic efficiency (CE) of Zn anode. However, the artificial layers built by *ex-situ* methods are generally not homogeneous enough to completely avoid the electrolyte invasion. More problematically, the anode volume change during Zn plating/stripping process can ruin the uncompacted layers, which severely limits their practical application in the case of high charge/discharge depth (>2 mAh cm^{-2}). Electrolyte additives such as organic molecules/polymers and metal ions have been utilized to suppress the side reactions and restrict the Zn dendrite growth, which is enabled by interface absorption and/or electrostatic shielding.

[36] Unfortunately, the polarity-induced molecule absorption is far from strong enough to achieve a thorough surface coverage of Zn anode, while the electrostatic shielding of metal ions plays a limited role to suppress HER and prevent the formation of by-products. [37] Upon recognizing the nature of zinc plating is a typical redox process at the zinc-electrolyte interface, the interfacial charge state can essentially be utilized to guide Zn^{2+} adsorption/diffusion from the kinetics perspective.

From the point of view in regulating zinc-electrolyte interfacial charge states, an interface charge engineering strategy is proposed by introducing amino acid additive to achieve highly reversible zinc plating/stripping. The positively charged amino acid such as arginine (Arg) is verified to be preferentially adsorbed on the surface of bulk Zn anode, initiating a self-adaptive zinc-electrolyte interface with strong steric hindrance, which effectively hinders water adsorption and guides uniform zinc deposition. Consequently, bulk Zn anode achieves an ultra-long stable cycling up to 2200 hours at a high current density of 5 mA cm^{-2} and an areal capacity of 4 mAh cm^{-2}. Moreover, such self-adaptive zinc-electrolyte interface enables AZIB full cells with MnO_2 cathode achieving long-term stable cycling.

2. Results and discussion

The key of this interface charge engineering strategy is to regulate zinc-electrolyte interface charge states by harnessing the electrostatic absorption of amino acids. Three typical hydrophile amino acids with varied types of electric charge in mildly acidic $ZnSO_4$ electrolyte (pH=5) were selected to investigate the absorption behaviors. **Figure 1**a and 1b show the adsorption model of amino acids and the corresponding adsorption energy through density functional theory (DFT) calculation. The highest adsorption energy calculated belongs to the positively charged arginine (Arg), whereas the negatively charged glutamate (Glu) exhibits the lowest value. Furthermore, the adsorption energy of Arg is calculated to be much higher than those values of H_2O and Zn, indicating that Arg molecules will be preferentially adsorbed on the Zn surface and guide Zn^{2+} flux during the plating process, which fulfils a passive role in isolating water adsorption to prevent HER and restricting Zn dendrite growth.

To further assess the electrostatic adsorption in terms of positive charge, Arg/Glu are modulated with positively/negatively charged and neutral (uncharged) states to investigate the difference in adsorption energy (the inset of Figure 1b), which clearly shows that positive charge will boost the interface adsorption regardless of the species of amino acids. Considering the mildly acidic environment of $ZnSO_4$ electrolyte, positively charged Arg additive is chosen for the subsequent electrochemical analysis. The Zeta potential measurement of Zn powders

(Figure S1) clearly verifies the strong electrostatic absorption of Arg molecules on the Zn surface, as the potential value increases from -27.4 to 8.23 mV with the addition of Arg. We further examine the adsorption behaviors of Arg by performing electrochemical impedance spectroscopy (EIS) tests at different potentials (Figure 1d), where the $ZnSO_4$ solution has been replaced by Na_2SO_4 solution to avoid the interference of faraday current. It is found that the surface capacitance is obviously decreased upon the Arg introduction, further addressing the strong electrostatic adsorption of Arg on the surface of Zn metal. To further illustrate the self-adaptability of the Arg adsorption, cyclic voltammetry (CV) curve of Zn symmetric cell in 0.1 M Arg solution is shown in Figure S2. A typical capacitive absorption behavior is verified with no redox peak observed, indicating that the zinc-electrolyte interface is dynamic during the Zn plating/stripping process. Such self-adaptive absorption layer of Arg can effectively adjust the interface charge states of Zn anode and therefore substantially affect the whole Zn plating/stripping process.

The chemical stability of Zn in the electrolyte with Arg additive was further investigated by immersing Zn metal in electrolytes as shown in Figure S3a-h. In comparison to the bare $ZnSO_4$ electrolyte, the Arg-added one distinctly restricts the surface corrosion, as a smooth surface morphology is observed after soaking the Zn for 5 days in the electrolyte with an Arg concentration up to 0.1 M. The ionic conductivity of above electrolytes (Figure S3i) shows a slight decrease with the increase of the Arg concentration. Hence, considering the optimal cycle life (Figure S3j), electrolyte containing 0.1 M Arg (named as $ZnSO_4$+Arg) is taken for the further tests. Symmetrical cell with galvanostatic method (1 mA cm^{-2} and 1 mAh cm^{-2}, Figure 1c) was used to test the stability of Zn anode in bare $ZnSO_4$ electrolyte and amino acid-added electrolytes. Compare to the bare $ZnSO_4$ electrolyte and electrolytes with Glu/Ser additives, the cell with Arg additive can achieve unprecedent cycle life up to 2950 hours and beyond at lower current density and areal capacity (0.32 mA cm^{-2}, 0.32 mAh cm^{-2}, over 3900 hours, Figure S4), revealing a fact that Arg additive can maximize the cycle life of bulk Zn anode under the same testing conditions.

To unveil the suppression of side reactions upon interfacial adsorption of charged Arg molecules, linear sweep voltammetry (LSV) scans were carried out as shown in **Figure 2**c. 3 M $ZnSO_4$ solution was replaced by 1 M Na_2SO_4 one to avoid the interference of zinc deposition reaction. Notably, the initial potential for HER decreases about 85 mV with Arg additive, suggesting the increased HER polarization and suppressed water adsorption. The phenomena can also be verified through linear polarization as shown in Figure 2d. Compared with bare $ZnSO_4$ electrolyte, Zn corrosion potential in $ZnSO_4$+Arg electrolyte increases and the corrosion

current density is reduced by 88.1 μA cm^{-2}, suggesting that the corrosion of Zn anode is largely impeded. [38] At a low current density, it is well known that, side-reactions other than dendrite growth will become the primary reason for cell failure. [19] To identify the inhibition effect for side-reactions, symmetrical cells are tested at a small current density of 0.1 mA cm^{-2} and areal capacity of 1 mAh cm^{-2}. The life span of Zn electrode is greatly extended with Arg additive (Figure 2f) for more than 700 hours stable cycling, while the cell in the bare $ZnSO_4$ shows voltage fluctuations after 150 hours due to the severe side reactions. *In-situ* optical microscopic observation during cycling provides an intuitive view on the inhibition of hydrogen evolution and surface corrosion in $ZnSO_4$+Arg electrolyte (Figure 2a, b and Video S1). In bare $ZnSO_4$ electrolyte, small gas bubbles emerge on the flat surface of Zn electrode in the first cycle, which develops heavily along with loose deposits accumulated after 20 cycles. On the contrary, there is no obvious gas evolution and loose deposits on the Zn electrode cycled in $ZnSO_4$+Arg electrolyte. X-ray diffraction (XRD) results (Figure 2e) provide the same verdict that no miscellaneous peaks appeared in $ZnSO_4$+Arg electrolyte after the zinc plating process. In contrast, Zn in bare $ZnSO_4$ electrolyte shows extra peaks at 16.6 °, 21.1 ° and 23.0 ° corresponding to the formation of $Zn_4SO_4(OH)_6 \cdot 5H_2O$ by-products (PDF #39-0688), which manifests the inhibited side reactions in $ZnSO_4$+Arg electrolyte. X-ray photoelectron spectroscopy (XPS) analysis of bare Zn and Zn anodes cycled in bare $ZnSO_4$ electrolyte and Arg-added one is conducted as shown in Figure S5. It can be seen that the Zn 2p peaks located at 1022.05 and 1045.15 eV show no shift, indicating the maintenance of the chemical environment of Zn deposits in both electrolytes.[29] Compared with the Zn anode cyled in $ZnSO_4$+Arg, the S 2p peaks located at 168.7 eV and 169.9 eV corresponding to the formation of ZSH as observed in XRD analysis,[39] indicating the severe side reactions in bare $ZnSO_4$ electrolyte.

Dendrite growth is another major concern when design the Zn anode since it can degrade the electrochemical reversibility significantly. The morphology evolutions of Zn surface after different cycles are shown in **Figure 3**e and 3f. In bare $ZnSO_4$ electrolyte, the surface becomes coarse with porous structure even after only one cycle, which turns to be severely aggravated with the hexagonal nanosheets and the particles accumulation after 50 cycles. By comparison, a smooth Zn surface is well maintained in $ZnSO_4$+Arg electrolyte after 50 cycles. Since the dendrite formation will be more notorious under ultra-high areal capacity testing,[40,41] an extremely high capacity of 10 mAh cm^{-2} is plated to further study the restriction of dendrite growth in $ZnSO_4$+Arg electrolyte (Figure S6, S7). The Zn electrode maintains smooth surface with a dense and uniform deposition as observed in the cross-sectional image. In contrast, large

quantities of hexagonal nanosheets are formed on the electrode surface, which leads to thick and loose deposits from the cross-sectional view. EDS mapping in Figure S7 shows that hexagonal dendrites and large clusters plate in bare $ZnSO_4$ electrolyte due to the associated growth of dendrite and ZSH by-products, while no obvious signals corresponding to O/S elements are observed for the Zn electrode in $ZnSO_4$+Arg electrolyte. *In-situ* optical microscopy is also carried out to characterize Zn plating process (Figure S8, Video S2), Cu wire was used as substrate and current is set as 10 mA. In bare $ZnSO_4$ electrolyte, Zn plating shows obviously spiked growth and size of dendrite continuously increases. On the contrary, benefitting from the self-adaptive zinc-electrolyte interface, spherical growth is observed for the Zn plating in $ZnSO_4$+Arg electrolyte.

To study the impact of Arg absorption on zinc plating/stripping, cyclic voltammetry (CV) scans were performed as shown in Figure 3a. In general, the nucleation process has a crossover point (A). The difference between potentials (B/C) and A corresponds to the nucleation overpotential, which obeys the following equation: [42]

$$r_{crit} = 2\frac{\gamma V_m}{F|\eta|} \quad (1)$$

Where γ is the surface energy of the anode-electrolyte interface, V_m is the molar volume of Zn, F is the Faraday constant and η is the nucleation overpotential. This equation indicates that the higher overpotential is, the finer particles of Zn deposition tends to form. Compared with bare $ZnSO_4$ electrolyte, the overpotential in $ZnSO_4$+Arg electrolyte is increased by nearly 30 mV, making Zn^{2+} plating more prone to grow in small nuclei. The charge transfer resistance and nucleation overpotential in symmetric cells (Figure S9 and S10) are both increased with the addition of Arg, further suggesting the hindered Zn^{2+} transfer kinetics. This can be attributed to the strong steric hindrance of charged Arg adsorption layer, which will guide the uniform Zn^{2+} ion flux on the Zn anode surface. In a further step, a negative overpotential of -150 mV is applied to Zn electrode to test chronoamperometry curve (Figure 3b). In bare $ZnSO_4$ electrolyte, the current density is continuously increasing, suggesting a continuous 2D diffusion process. [43,44] Conversely, the change in current density is slowed down beyond the initial 100 s with the addition of Arg in the electrolyte, indicating the hindered Zn^{2+} 2D diffusion. Such verdict is also verified by DFT calculation, as shown in Figure 3g and 3h, with the adsorption of Arg on anode surface, Zn migration energy at different positions is significantly increased, which also indicates the inhibition of 2D diffusion process.

Therefore, the guided uniform Zn^{2+} ion flux and the restrained 2D diffusion make Zn^{2+} in contact with anode surface tend to react directly to avoid consecutive dendrite growth. Simultaneously, charged Arg molecules on protrusions also play a beneficial role in the

inhibition of dendrite growth through electrostatic shielding.[45] To further testify the dendrite restriction effect, symmetrical cells at various capacity (10 mAh cm^{-2} and 20 mAh cm^{-2}, respectively, Figure 3c, d) were tested, short circuit occurs rapidly for the cells in bare $ZnSO_4$ electrolyte (less than 30 hours) due to the severe dendrite growth. On the opposite, the cell with $ZnSO_4$+Arg electrolyte can support more than 200 hours even at an ultra-high areal capacity of 20 mAh cm^{-2}, resulted by the self-adaptive feature and steric hindrance of Arg adsorption.

The promotion effect of Arg additive is illustrated in **Figure 4**a. In bare $ZnSO_4$ electrolyte, Zn^{2+} randomly absorbs on the zinc surface and migrate to the tip of nucleation sites during the plating process, leading to dendrite formation. Simultaneously, side reactions including HER and by-products formation will inevitably occur due to the competitive H_2O adsorption on the anode surface, resulting in poor reversibility of Zn anode. Nevertheless, with the Arg additive, Zn metal surface is occupied by Arg molecules through absorption, which can obstruct H_2O adsorption and restrict dendrite growth, creating a stable zinc-electrolyte interface. That is, with the continuous deposition of Zn^{2+}, the adsorbed Arg is still anchored at interface in a self-adaptive manner, thereby yielding a smooth plating behaviour.

To evaluate the cycling stability of Zn anode in $ZnSO_4$+Arg electrolyte for the practical application, an ultra-high testing condition with the current density of 5 mA cm^{-2} and areal capacity of 4 mAh cm^{-2} (Figure 4b) are applied when testing the symmetric cells. The insert of Figure 4b reveals the details of voltage profiles during Zn plating/stripping process under the different cycling periods. In bare $ZnSO_4$ electrolyte, the cell fails only after 70 hours, while $ZnSO_4$+Arg electrolyte can ensure a long-term stable cycling for more than 2200 hours. Even at 10 mA cm^{-2} and 4 mAh cm^{-2}, which largely exceeds the general requirements for practical application, stable cycling up to nearly 900 hours is recorded indicating the self-adaptive feature of interface adsorption to accommodate deep and fast charge/discharge, which is among the best life span reported under similar testing conditions so far (Figure 4d, table S1). By assembling the Zn-Ti cell, the CE in $ZnSO_4$+Arg electrolyte is recorded with an average value of 98.3% (Figure 4e-g), unveiling the good reversibility of Zn plating/stripping. By contrast, the CE in bare $ZnSO_4$ electrolyte fluctuated significantly and the cut-off voltage cannot be reached after 60 cycles due to the severe side reactions. Voltage curve under continuous charging in symmetrical cell (Figure S11) shows severe fluctuation in bare $ZnSO_4$ electrolyte, in contrast, a high Zn extraction rate is obtained in $ZnSO_4$+Arg electrolyte which indicates the reversibility of electrode is greatly improved. [46-48] The results from above electrochemical tests strongly prove the effectiveness of Arg additive, which can be ascribed the formation of stable and self-adaptive interface layer due to the strong electrostatic adsorption of Arg molecules.

Such self-adaptive zinc-electrolyte interface can be constructed by other positively charged amino acid such as lysine (Lys) and similar promotion effect is demonstrated with long cycle life and high CE in symmetric cells (Figure S12), demonstrating the universal applicability of the interface charge engineering strategy.

As a proof-of-concept, AZIB is evaluated in $ZnSO_4$+Arg electrolyte by selection of a conventional MnO_2 cathode material synthesized according to the literature method. [23] The nanorod-like α-MnO_2 can be verified by XRD (Figure S13) and SEM (Figure S14). The full cells were tested with the addition of 0.1M $MnSO_4$ to avoid the dissolution of cathode Mn^{2+} in the above electrolytes. The CV curves of full cells (Figure S15) presents typical redox peaks of MnO_2 in both bare $ZnSO_4$ and $ZnSO_4$+Arg electrolytes, indicating that the redox process of MnO_2 remains unchanged with Arg introduction. Due to the adsorption of Arg, Zn|$ZnSO_4$+Arg|MnO_2 cell shows a minor increase in voltage polarization, which is identical to the charge-discharge curves in **Figure 5**a and 5b. The cycling performance and corresponding CEs of cells are tested at 500 mA g^{-1} (Figure 5c), where the capacity of Zn|$ZnSO_4$|MnO_2 cell experiences abrupt drop after only 120 cycles. At this current density (about 1 mA cm^{-2} for anode), the continuous dendrite growth on the anode will cause short circuit after about 150 hours, which is consistent with the cycle life of symmetrical cell. On the contrary, Zn|$ZnSO_4$+Arg|MnO_2 full cell exhibits superior cycling performance with an average CE of 99.7% and capacity retention of more than 83% over 200 cycles, which emphasize the key role of Arg adsorption in benefiting the zinc plating/stripping. Additionally, full cell also shows a high rate capability with Arg additive (Figure S16). The surface morphology of Zn anodes after 50 cycles in different electrolytes are shown in Figure S17, holes and prominences occurr in bare $ZnSO_4$ electrolyte and a smooth surface can still be maintained in $ZnSO_4$+Arg electrolyte.

3. Conclusion

In this work, we demonstrate an interface engineering approach to regulate the zinc-electrolyte interface charge states through electrostatic absorption of positively charged Arg additive, to achieve highly reversible Zn anode. The adsorbed Arg molecules can form a self-adaptive interface which maintain stable during Zn plating/stripping process and effectively prevent H_2O adsorption and hinder the 2D diffusion of Zn^{2+}, thereby suppressing side reactions and dendrite growth. This self-adaptive zinc-electrolyte interface enables a stable and highly reversible average plating/stripping CE of 98.26% over 300 cycles. This strategy effectively extends Zn electrode lifespan to nearly 2200 hours of symmetrical cells under ultra-high current density and areal capacity of 5 mA cm^{-2} and 4 mAh cm^{-2}. Moreover, the application potential

of $ZnSO_4$+Arg electrolyte is validated by Zn|MnO_2 full cell which shows the preferable cycling stability.

Supporting Information
Supporting Information is available from the Wiley Online Library or from the author.

Acknowledgements

This work was supported by the National Natural Science Foundation of China (51722105), Zhejiang Provincial Natural Science Foundation of China (LR18B030001), and National Key Research and Development Program (2019YFE0111200).

Received: ((will be filled in by the editorial staff))
Revised: ((will be filled in by the editorial staff))
Published online: ((will be filled in by the editorial staff))

References

[1] J. B. Goodenough, *Nat. Electron*. **2018**,*1*,204-204.

[2] F. Wu and G. Yushin, *Energy Environ. Sci.* **2017**, *10*, 435-459.

[3] T. C. Wanger, *Conserv. Lett.* **2011**, *4*, 202-206.

[4] X. Li, J. Liang, X. Yang, K. R. Adair, C. Wang, F. Zhao and X. Sun, *Energy Environ. Sci.* **2020**, *13*, 1429-1461.

[5] M.-C. Lin, M. Gong, B. Lu, Y. Wu, D.-Y. Wang, M. Guan, M. Angell, C. Chen, J. Yang, B.-J. Hwang and H. Dai, *Nature* **2015**, *520*, 324-328.

[6] H. Kim, J. Hong, K.-Y. Park, H. Kim, S.-W. Kim and K. Kang, *Chem. Rev.* **2014**, *114*, 11788-11827.

[7] D. Bin, F. Wang, A. G. Tamirat, L. Suo, Y. Wang, C. Wang and Y. Xia, *Adv. Energy Mater.* **2018**, *8*, 1703008.

[8] H. D. Yoo, I. Shterenberg, Y. Gofer, G. Gershinsky, N. Pour and D. Aurbach, *Energy Environ. Sci.* **2013**, *6*, 2265-2279.

[9] M. Song, H. Tan, D. Chao and H. J. Fan, *Adv. Funct. Mater.* **2018**, *28*, 1802564

[10] A. Ponrouch, C. Frontera, F. Bardé and M. R. Palacín, *Nat. Mater.* **2016**, *15*, 169-172.

[11] D. Kundu, B. D. Adams, V. Duffort, S. H. Vajargah and L. F. Nazar, *Nat. Energy* **2016**, *1*, 16119.

[12] J. F. Parker, C. N. Chervin, I. R. Pala, M. Machler, M. F. Burz, J. W. Long and D. R. Rolison, *Science* **2017**, *356*, 415-418.

[13] L. E. Blanc, D. Kundu and L. F. Nazar, *Joule* **2020**, *4*, 771-799.

[14] G. Fang, J. Zhou, A. Pan and S. Liang, *ACS Energy Lett.* **2018**, *3*, 2480-2501.

[15] Z. Wang, J. Huang, Z. Guo, X. Dong, Y. Liu, Y. Wang and Y. Xia, *Joule* **2019**, *3*, 1289-1300.

[16] H. Pan, Y. Shao, P. Yan, Y. Cheng, K. S. Han, Z. Nie, C. Wang, J. Yang, X. Li, P. Bhattacharya, K. T. Mueller and J. Liu, *Nat. Energy* **2016**, *1*, 16039.

[17] B. Tang, L. Shan, S. Liang and J. Zhou, *Energy Environ. Sci.* **2019**, *12*, 3288-3304.

[18] T. Shoji, M. Hishinuma and T. Yamamoto, *J. Appl. Electrochem.* **1988**, *18*, 521-526.

[19] Q. Yang, G. Liang, Y. Guo, Z. Liu, B. Yan, D. Wang, Z. Huang, X. Li, J. Fan and C. J. A. M. Zhi, *Adv. Mater.* **2019**, *31*, 1903778.

[20] W. Du, E. H. Ang, Y. Yang, Y. Zhang, M. Ye and C. C. Li, *Energy & Energy Environ. Sci.* **2020**, *13*, 3330-3360.

[21] C. Han, W. Li, H. K. Liu, S. Dou and J. Wang, *Nano Energy* **2020**, *74*, 104880.

[22] C. Li, X. Xie, S. Liang and J. Zhou, *Energy Environ. Mater.* **2020**, *3*, 146-159.

[23] L. Kang, M. Cui, F. Jiang, Y. Gao, H. Luo, J. Liu, W. Liang and C. Zhi, *Adv. Energy Mater.* **2018**, *8*, 1801090.

[24] K. Zhao, C. Wang, Y. Yu, M. Yan, Q. Wei, P. He, Y. Dong, Z. Zhang, X. Wang and L. Mai, *Adv. Mater. Interfaces* **2018**, *5*, 1800848.

[25] P. Liang, J. Yi, X. Liu, K. Wu, Z. Wang, J. Cui, Y. Liu, Y. Wang, Y. Xia and J. Zhang, *Adv. Funct. Mater.* **2020**, *30*, 1908528.

[26] J. Hao, X. Li, S. Zhang, F. Yang, X. Zeng, S. Zhang, G. Bo, C. Wang and Z. Guo, *Adv. Funct. Mater.* **2020**, *30*, 2001263.

[27] Q. Yang, Y. Guo, B. Yan, C. Wang, Z. Liu, Z. Huang, Y. Wang, Y. Li, H. Li, L. Song, J. Fan and C. Zhi, *Adv. Mater.* **2020**, *32*, 2001755.

[28] Z. Zhao, J. Zhao, Z. Hu, J. Li, J. Li, Y. Zhang, C. Wang and G. Cui, *Energy Environ. Sci.* **2019**, *12*, 1938-1949.

[29] J. Hao, B. Li, X. Li, X. Zeng, S. Zhang, F. Yang, S. Liu, D. Li, C. Wu and Z. Guo, *Adv. Mater.* **2020**, *32*, 2003021.

[30] A. Mitha, A. Z. Yazdi, M. Ahmed and P. Chen, *ChemElectroChem* **2018**, *5*, 2409-2418.

[31] Z. Hou, X. Zhang, X. Li, Y. Zhu, J. Liang and Y. Qian, *J. Mater. Chem. A* **2017**, *5*, 730-738.

[32] K. E. K. Sun, T. K. A. Hoang, T. N. L. Doan, Y. Yu, X. Zhu, Y. Tian and P. Chen, *ACS Appl. Mater. Interfaces* **2017**, *9*, 9681-9687.

[33] W. Xu, K. Zhao, W. Huo, Y. Wang, G. Yao, X. Gu, H. Cheng, L. Mai, C. Hu and X. Wang, *Nano Energy* **2019**, *62*, 275-281.

[34] Q. Zhang, J. Luan, L. Fu, S. Wu, Y. Tang, X. Ji and H. Wang, *Angew. Chem. Int. Ed.* **2019**, *58*, 15841-15847.

[35] F. Wang, O. Borodin, T. Gao, X. Fan, W. Sun, F. Han, A. Faraone, J. A. Dura, K. Xu and C. Wang, *Nat. Mater.* **2018**, *17*, 543-549.

[36] F. Ding, W. Xu, G. L. Graff, J. Zhang, M. L. Sushko, X. Chen, Y. Shao, M. H. Engelhard, Z. Nie, J. Xiao, X. Liu, P. V. Sushko, J. Liu and J.-G. Zhang, *J. Am. Chem. Soc.* **2013**, *135*, 4450-4456.

[37] F. Wan, L. Zhang, X. Dai, X. Wang, Z. Niu and J. Chen, *Nat. Commun.* **2018**, *9*, 1656.

[38] M. Abdallah, *Corros. Sci.* **2003**, *45*, 2705-2716.

[39] X. Guo, Z. Zhang, J. Li, Ni. Luo, G. Chai, T. S. Miller, F. Lai, P. Shearing, D. J. L. Brett, D. Han, Z. Weng, G. He, and I. P. Parkin, *ACS Energy Let.* **2021,** 6, 395-403.

[40] A. Naveed, H. Yang, J. Yang, Y. Nuli, J. Wang, *Angew. Chem. Int. Ed.* **2019**, *58*, 2760.

[41] Q. Yang, Q. Li, Z. Liu, D. Wang, Y. Guo, X. Li, Y. Tang, H. Li, B. Dong and C. Zhi, *Adv. Mater.* **2020**, *32*, 2001854.

[42] A. Pei, G. Zheng, F. Shi, Y. Li and Y. Cui, *Nano Lett.* **2017**, *17*, 1132-1139.

[43] G. Trejo, H. Ruiz, R. O. Borges and Y. Meas, *J. Appl. Electrochem.* **2001**, *31*, 685-692.

[44] A. Bayaguud, X. Luo, Y. Fu and C. Zhu *ACS Energy Let.* **2020**, *5*, 3012-3020.

[45] Z. Chen, H. Chen, Y.i Che, L. Cheng, H. Zhang, J. Chen, F. Xie, N. Wang, Y. Jin, and H. Meng. ACS *Sustain. Chem. Eng.* **2021**, 9, 6855-6863

[46] F. Zhou, Z. Li, Y.-Y. Lu, B. Shen, Y. Guan, X.-X. Wang, Y.-C. Yin, B.-S. Zhu, L.-L. Lu, Y. Ni, Y. Cui, H.-B. Yao and S.-H. Yu, *Nat. Commun.* **2019**, *10*, 2482.

[47] S. Liu, L. Deng, W. Guo, C. Zhang, X. Liu and J. Luo, *Adv. Mater.* **2019**, *31*, 1807585.

[48] K. Cao, Q. Ma, F. Tietz, B. B. Xu, M. Yan and Y. Jiang, *Sci. Bull.* **2020**, *6*, 005.

[49] Y. Zeng, X. Zhang, R. Qin, X. Liu, P. Fang, D. Zheng, Y. Tong and X. Lu, *Adv. Mater.* **2019**, *31*, 1903675.

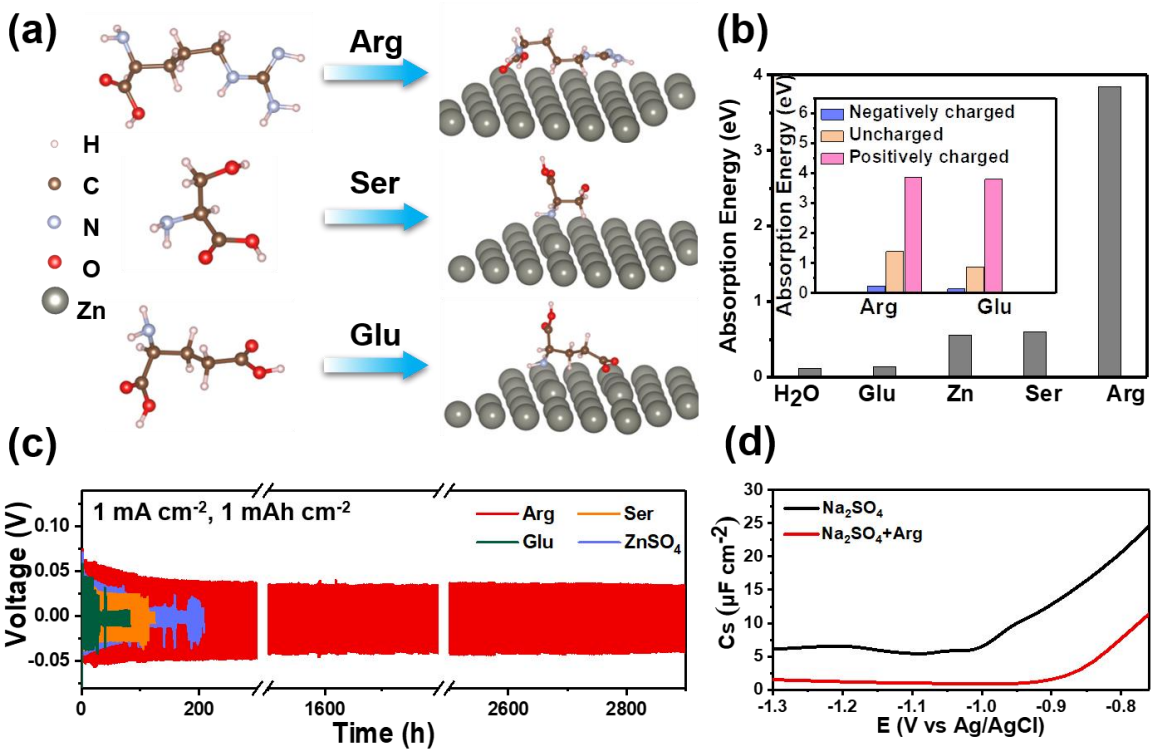

Figure 1. (a) Density functional theory (DFT) calculation models of Arg, Ser and Glu. (b) Absorption energy of H_2O, Glu, Zn, Ser and Arg on Zn surface in mildly acidic electrolyte, respectively. Inset is absorption energy of Arg and Glu with positively charged, uncharged and negatively charged on Zn surface, respectively. (c) Cycling stability of symmetrical cells with/without amino acid additives at 1 mA cm^{-2}, 1 mAh cm^{-2}. (d) Differential capacitance curve for Zn in Na_2SO_4 solution with/without Arg additive.

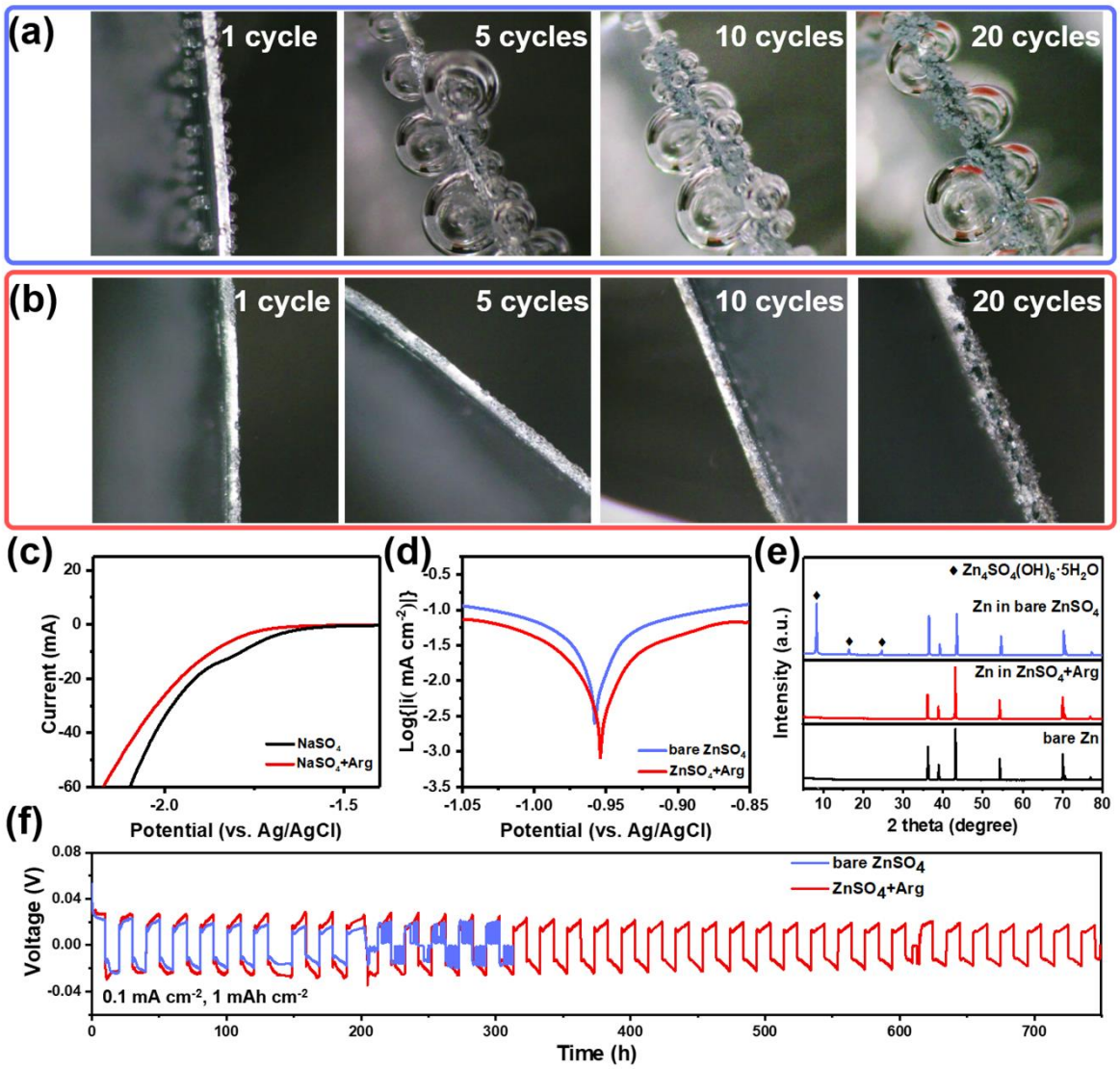

Figure 2. In-situ optical microscope image of Zn electrode at 1st, 5th, 10th and 20th cycle (a) in bare $ZnSO_4$ electrolyte and (b) in $ZnSO_4$+Arg electrolyte. (c) Linear sweep voltammetry (LSV) curve in 1 M Na_2SO_4 and 1 M Na_2SO_4+0.1 M Arg electrolyte. (d) Linear polarization curves in bare $ZnSO_4$ and $ZnSO_4$+Arg electrolyte. (e) X-ray diffraction (XRD) patterns of bare Zn and Zn electrodes after 10 mAh cm^{-2} Zn plating in two electrolytes. (f) Cycling stability of symmetrical cells at 0.1 mA cm^{-2}, 1 mAh cm^{-2}.

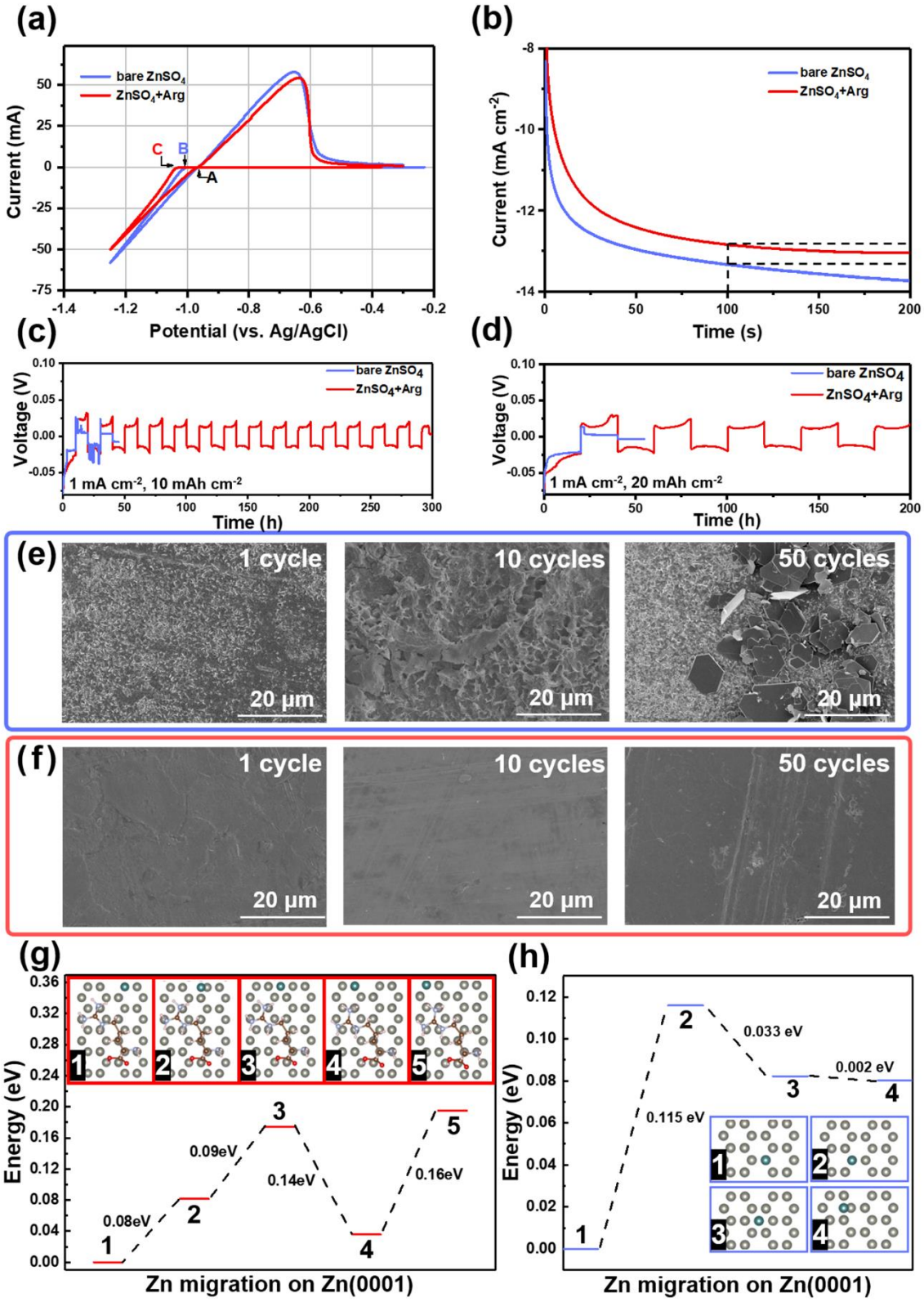

Figure 3. (a) Cyclic voltammograms (CVs) for Zn nucleation on Ti foil and (b) Chronoamperograms (CAs) of Zn in bare $ZnSO_4$ electrolyte and $ZnSO_4$+Arg electrolyte, respectively. Cycling stability of symmetrical cells (c) at 1 mA cm^{-2}, 10 mAh cm^{-2} and (d) 1 mA cm^{-2}, 20 mAh cm^{-2}. Surface morphology of Zn electrode at 1st, 10th and 50th cycle (e) in bare $ZnSO_4$ electrolyte and (f) in $ZnSO_4$+Arg electrolyte. Zn migration energy on Zn (0001): (g) Zn with Arg, (h) bare Zn, insets show the calculated migration positions.

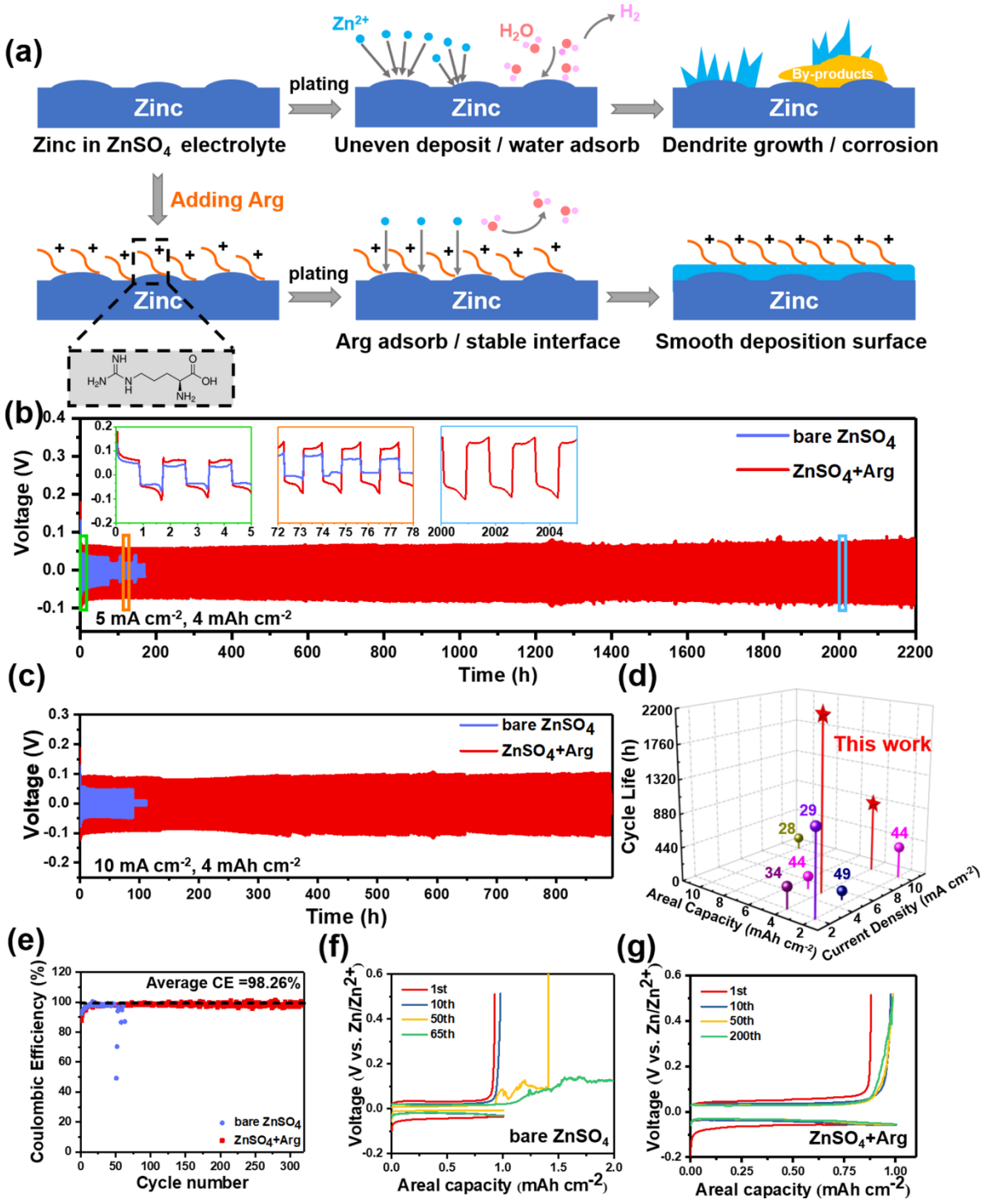

Figure 4. (a) Schematic illustration of Zn plating behavior with and without Arg additive. In bare $ZnSO_4$ electrolyte, uneven Zn plating and H_2O adsorption will lead to dendrite growth and side-reactions. In $ZnSO_4$+Arg electrolyte, a stable and self-adaptive interface adsorption of Arg can obtain a uniform Zn plating surface. Galvanostatic cycling of symmetrical cell in bare $ZnSO_4$ and $ZnSO_4$+Arg electrolyte at (b) 5 mA cm^{-2}, 4 mAh cm^{-2} (insets: the enlarge profiles of voltage curve) and (c) 10 mA cm^{-2}, 4 mAh cm^{-2}. (d) Comparison of cycling stability of symmetrical cell over 2 mA cm^{-2}, 2 mAh cm^{-2}. [28,29,34,44,49] (e) CEs of Zn plating/stripping on Ti foil in bare $ZnSO_4$ and $ZnSO_4$+Arg electrolyte at 1 mA cm^{-2} and capacity of 1 mAh cm^{-2} and the corresponding voltage profiles (f) and (g) at different cycles, respectively.

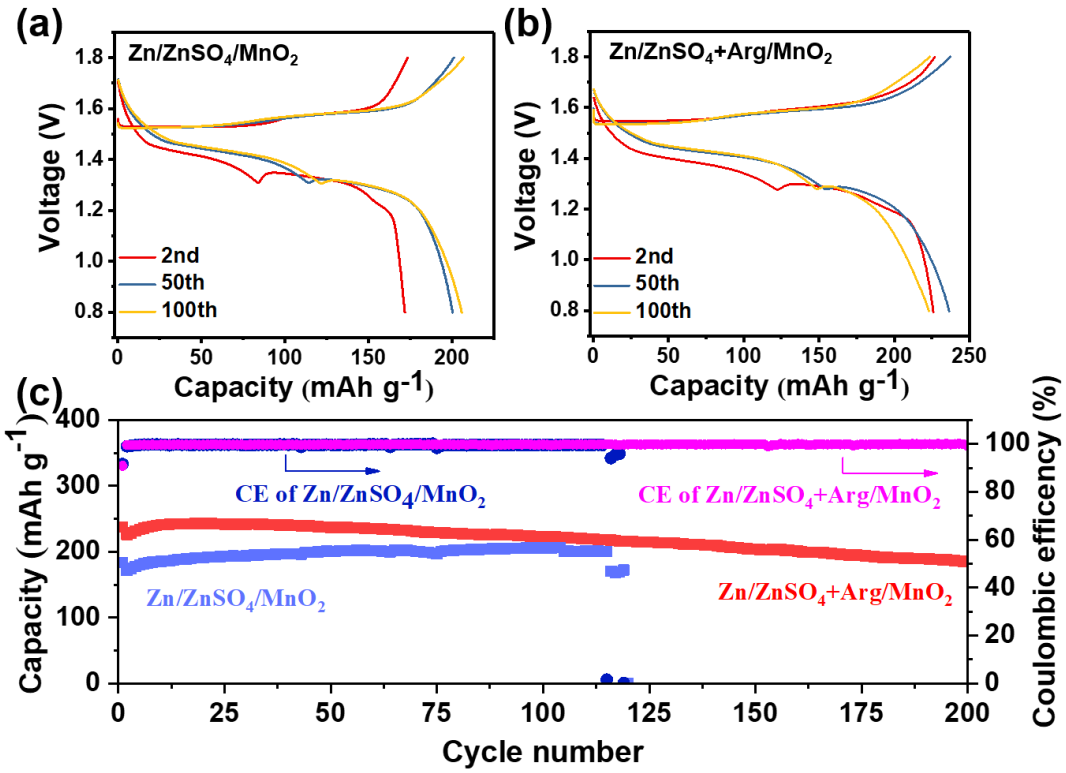

Figure 5. Electrochemical performance of full cells: (a,b) Galvanostatic charge-discharge profiles of $Zn/ZnSO_4/MnO_2$ and $Zn/ZnSO_4$+Arg/MnO_2 batteries at 2nd, 50th and 100th, respectively. (c) Long-term cycling performance and corresponding CEs at 500 mA g^{-1}.

Amino Acid-Induced Interface Charge Engineering Enables Highly Reversible Zn Anode

*Haotian Lu, Xuanlin Zhang, Minghe Luo, Keshuang Cao, Yunhao Lu, Ben Bin Xu, Hongge Pan, Kai Tao and Yinzhu Jiang**

ToC figure

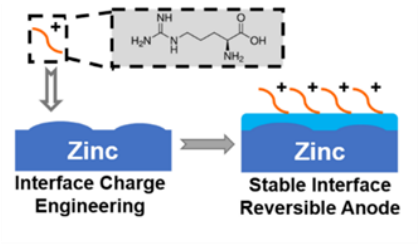

Although aqueous rechargeable zinc battery holds great promise in energy storage, dendrite growth and side reactions have long limited the advance of zinc metal anode in rechargeable zinc battery. Herein, an interface charge engineering strategy is proposed *via* amino acid additive to regulate zinc-electrolyte interface charge states in achieving highly reversible Zn plating/stripping process.

Supporting Information

Amino Acid-Induced Interface Charge Engineering Enables Highly Reversible Zn Anode

*Haotian Lu, Xuanlin Zhang, Minghe Luo, Keshuang Cao, Yunhao Lu, Ben Bin Xu, Hongge Pan, Kai Tao and Yinzhu Jiang**

Experimental Section

Electrolyte preparation: 3 mol L^{-1} $ZnSO_4$ electrolyte was obtained by dissolving zinc sulfate heptahydrate (Sinopharm Chemical Reagent Co., Ltd, Shanghai, China) in deionized water. Different kinds of amino acids (Arg, Glu, Ser, Aladdin) were added into $ZnSO_4$ electrolyte and adjusted electrolyte pH to 5 (±0.2) by sulfuric acid or zinc hydroxide, in which the addition amount of Glu and Ser was 0.1M and the addition amount of Arg was 0.01 M, 0.05 M, and 0.1 M respectively.

Preparation of MnO_2: MnO_2 was obtained from previous report. [1] Firstly, 4.74 g of $KMnO_4$ and 11.03 g of $Mn(CH_3COO)_2{\cdot}4H_2O$ (Sinopharm Chemical Reagent Co., Ltd) were dissolved into 40 mL deionized water separately. Then $Mn(CH_3COO)_2$ solution was slowly added into $KMnO_4$ solution and heated at 80 °C for 4 h. The obtained precipitates were filtered and washed with deionized water and dried at 80 °C for 12 h and were further annealed at 200 °C for 2 h in air.

DFT calculation: First-principles calculations based on density functional theory were performed via the Vienna ab-initio simulation package (VASP) [2,3] using the generalized gradient approximation (GGA) with the projected augmented wave (PAW) method. [4,5] Perdew-Burke-Ernzerh (PBE) [6] function was adopted for exchange-correlation functional. The energy cutoff for the plane wave basis expansion was set to 400 eV. The Brillouin zone was sampled by the Gamma-point for geometric optimization. The Grimme's method (DFT-D3) [7] was employed to incorporate the effects of van der Waals interactions. To minimize the interactions between the molecules, a supercell (13.801 Å×15.937 Å) of Zn(0001) surface with

five zinc layers and 20 Å vacuum were selected to simulate the adsorption systems. The bottom three-layer zinc atoms were fixed to describe the bulk properties, and the other atoms were fully relaxed until the Hellmann-Feynman force on each atom was less than 0.05 eV/Å. An extra electron was added to/extracted from this system to simulate the charged state of the amino acids. The adsorption energy (E_{ads}) of the amino acids on Zn(0001) surface was obtained by using the following equation:

$$E_{\text{ads}} = E_{\text{amino acid+Zn(0001)}} - E_{\text{amino acid}} - E_{\text{Zn(0001)}}$$

where $E_{\text{amino acid + Zn(0001)}}$ was the total energy of the adsorption systems. $E_{\text{amino acid}}$ was the energy of the optimized amino acid configurations and $E_{\text{Zn(0001)}}$ was the energy of the Zn(0001) surface. The migration energy is defined as the relative energy between adjacent high-symmetric zinc adsorption positions along the migration path.

Electrochemical measurements: The Neware BTS-5 test system was employed to obtain galvanostatic measurements of coin cells. Linear polarization, chronoamperometry (CA), linear sweep voltammetry (LSV), differential capacitance (DC) and cyclic voltammetry (CV) tests were carried on an CHI660C electrochemical workstation with three-electrode systems which Ti foil, Zn plate and Ag/AgCl adopted as working, counter and reference electrode. Electrochemical impedance (EIS) was carried out with symmetric cell. The corrosion current was calculated from Tafel fit system in electrochemical workstation. Ionic conductivities were tested by two blocking electrodes and calculated from equation: $\sigma = l/(R \cdot S)$. Where l represents the distance between electrodes, R represents the resistance from electrochemical impedance spectrum test, and S is the area of blocking electrodes. Differential capacitance curve was calculated from equation: $C = -(\omega Z_{im})^{-1}$. Where C is differential capacitance and ω is angular frequency and Z_{im} is the imaginary part of impedance, 1000 Hz was selected as specific frequency. To avoid electrochemical reaction, 0.1 M Na_2SO_4 was selected as solution.

Cell fabrication: CR2025 coin cells were assembled at air atmosphere for symmetrical cells, CE and full cell tests. Zn plates (Sinopharm Chemical Reagent Co., Ltd) and Ti foils (Shenzhen Kejing Star Technology) without further modification were cut in round coins with 8 mm radius and glass fiber filters were used as the separator. The symmetrical cells assembled with two identical Zn plates. Ti foil as working electrode and Zn plate as counter electrode were used to test CE. Cathode electrodes comprised MnO_2 (70 wt%), Super P carbon (20 wt%) and polyvinylidene fluoride (10 wt%) in N-methyl-2-pyrrolidone solvent were mixed and coated on Ti foils (10 μm thickness) by the doctor blading method. The electrodes were dried in vacuum drying oven at 80 °C overnight and mass load was about 2 mg cm^{-2}. This cathode and Zn plate anode were used to assemble full cells.

Materials characterization: Zeta potentials were obtained from Malvern Zetasizer Nano-ZS. X-ray diffraction (XRD) patterns were carried out on a Bruker D8 diffractometer equipped with Cu - K_α radiation, with 2θ range from 5° to 80°. X-ray photoelectron spectroscopy (XPS) spectres were carried out from Kratos AXIS Supra, all binding energies were corrected for the charge shift using C 1s peak at 284.8 eV. Surface morphology and element distribution images were obtained from scanning electron microscopy (SEM, HITACHI SU8010) and Oxford X-Max 80 EDX spectrometer. All these electrode samples were obtained in three-electrode electrochemical cells with Zn plates as both reference/counter electrodes and working electrodes. in-situ optical microscope video and images were obtained from a ZW-C200 optical microscope (Shenzhen Zhongwei Science and Technology Co. LTD).

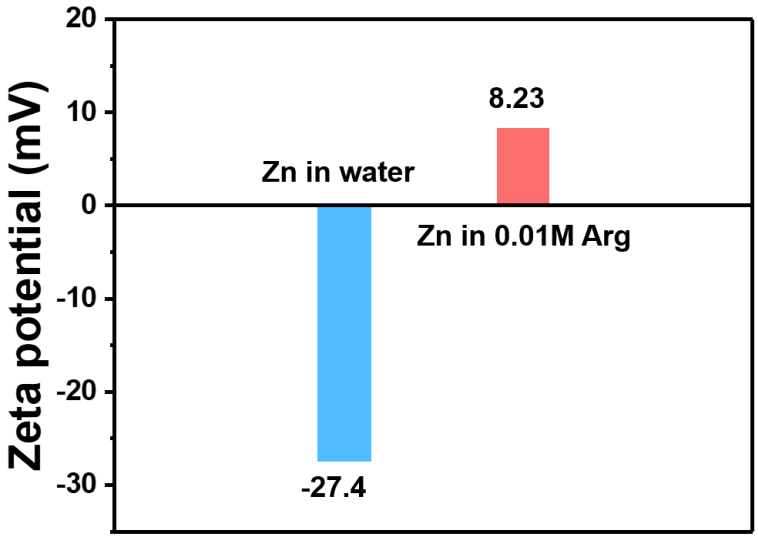

Figure S1. Zeta potential of Zinc powder with and without 0.01M Arg additive.

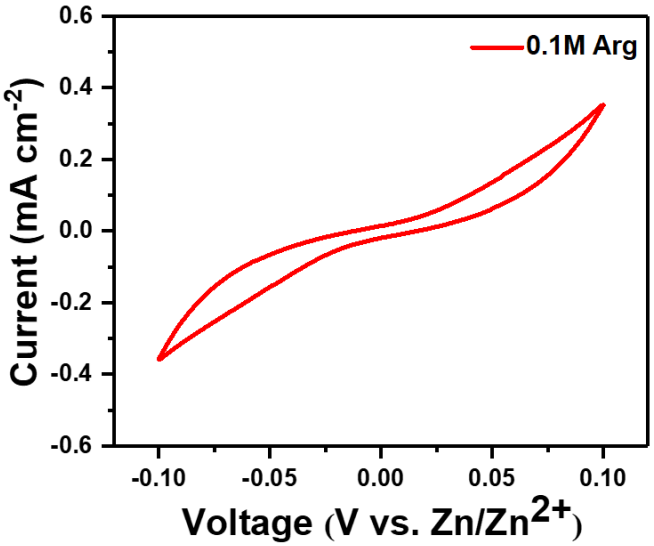

Figure S2. Cyclic voltammetry (CV) curve of Zn symmetric cell with 0.1M Arg solution at 5mV s^{-1}.

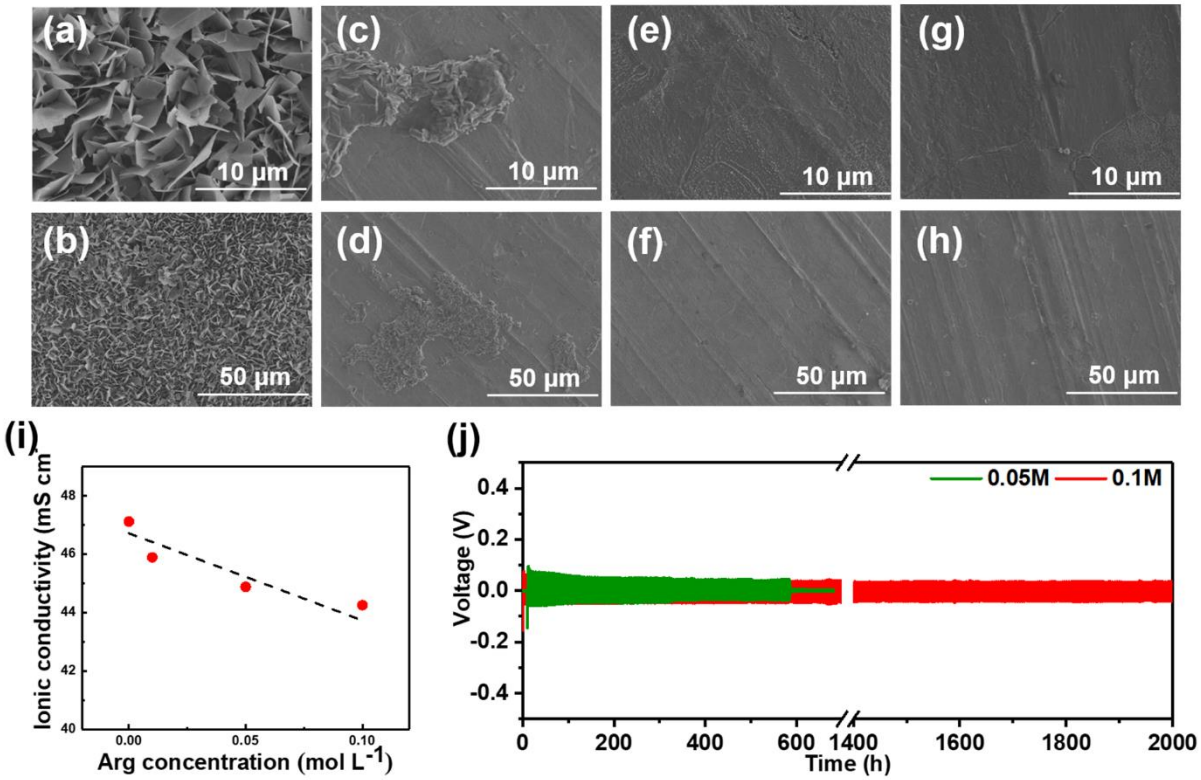

Figure S3. Surface morphology of Zn plate soaked 5 days: (a-b) in 3 M $ZnSO_4$. (c-d) with 0.01 M Arg additive. (e-f) with 0.05 M Arg additive. (g-h) with 0.1 M Arg additive. (i) Ionic conductivity of electrolytes with different Arg concentration. (j) Symmetrical cell test with different Arg concentration at 1 mA cm^{-2}, 1 mAh cm^{-2}.

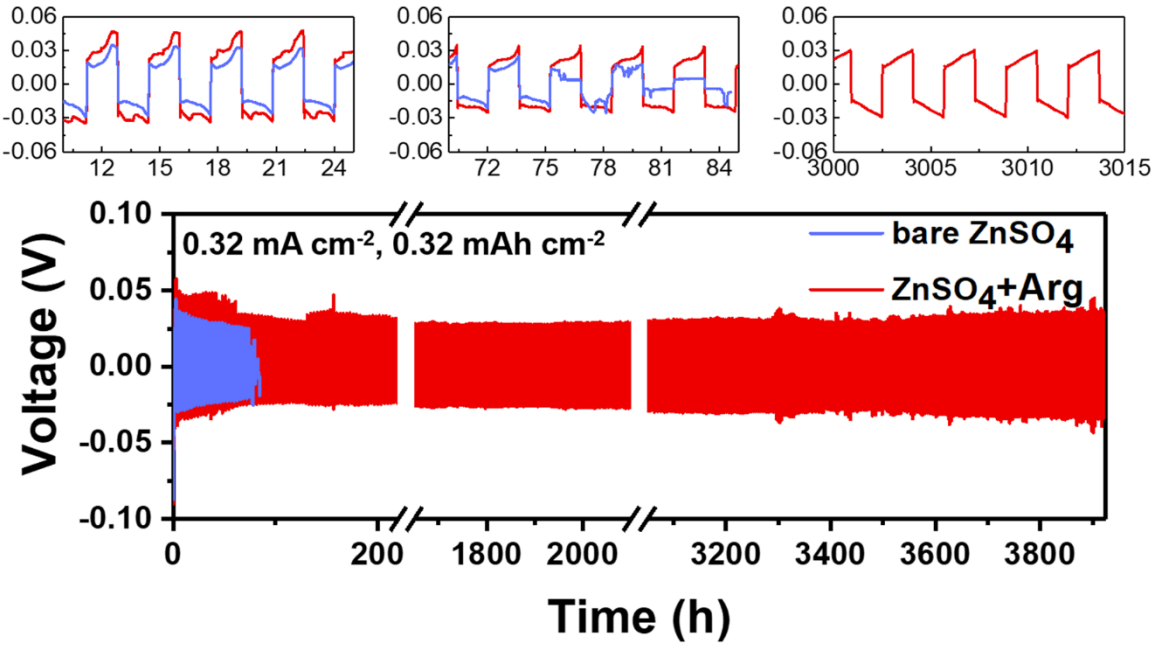

Figure S4. Galvanostatic cycling of symmetrical cell at 0.32 mA cm^{-2}, 0.32 mAh cm^{-2} and corresponding cycling details.

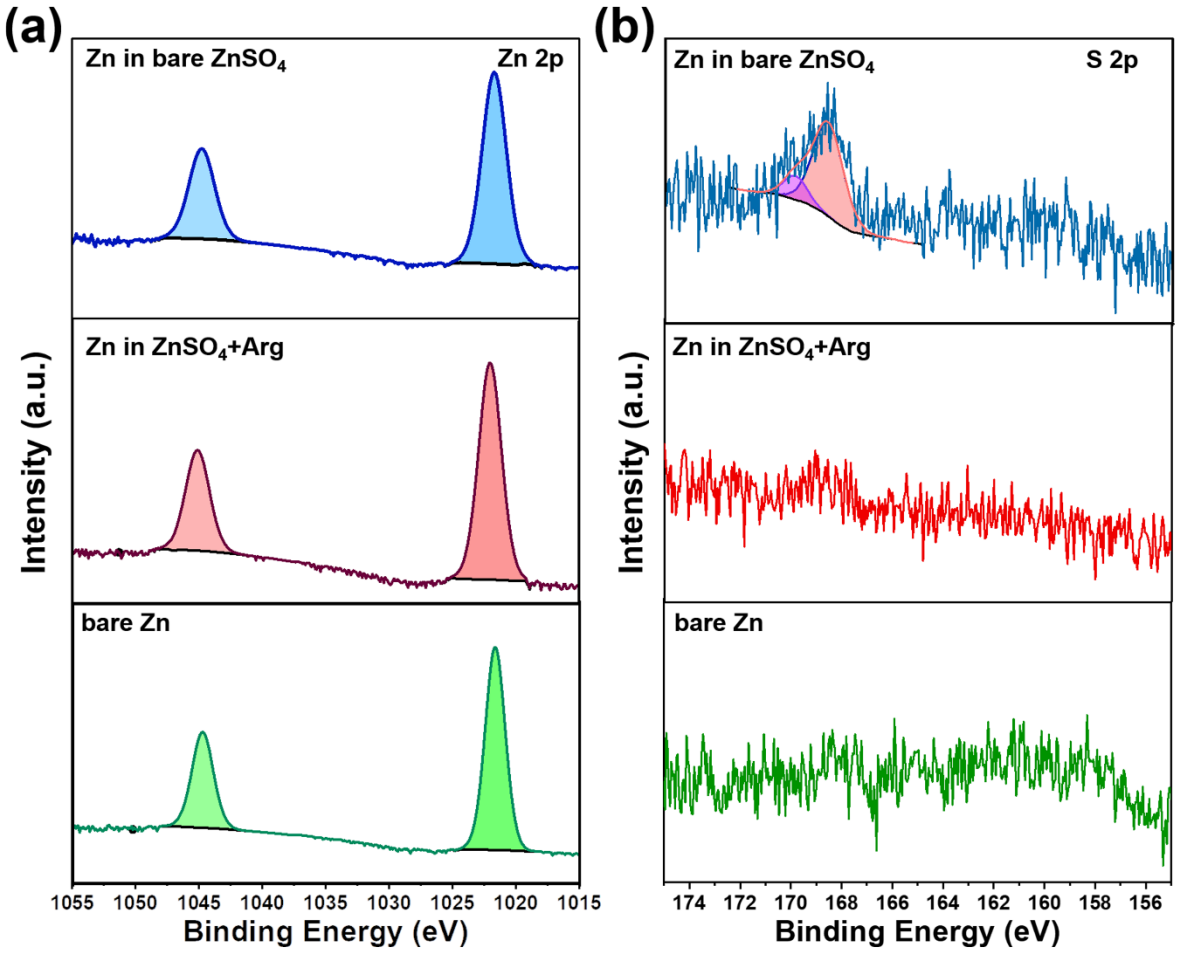

Figure S5. X-ray photoelectron spectroscopy (XPS) characterization of bare Zn, cycled Zn in bare $ZnSO_4$ and $ZnSO_4$+Arg, respectively: (a) Zn 2p spectra, (b) S 2p spectra.

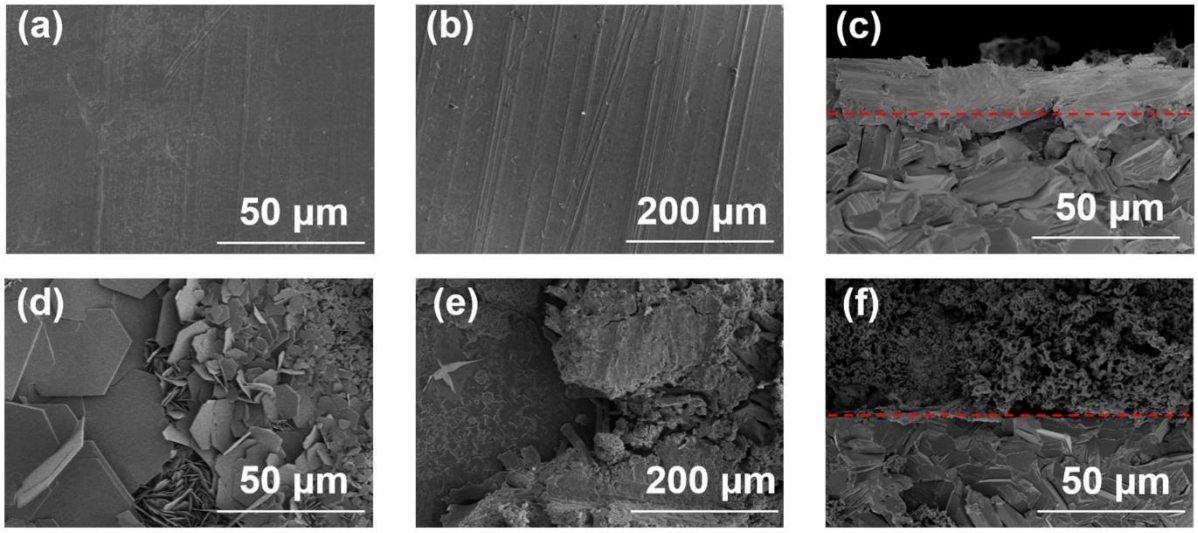

Figure S6. Surface and cross-sectional morphology of Zn electrode after 10mAh cm^{-2} Zn plating (1 mA cm^{-2} current density). (a-c) Zn in $ZnSO_4$+Arg electrolyte. (d-f) Zn in bare $ZnSO_4$ electrolyte.

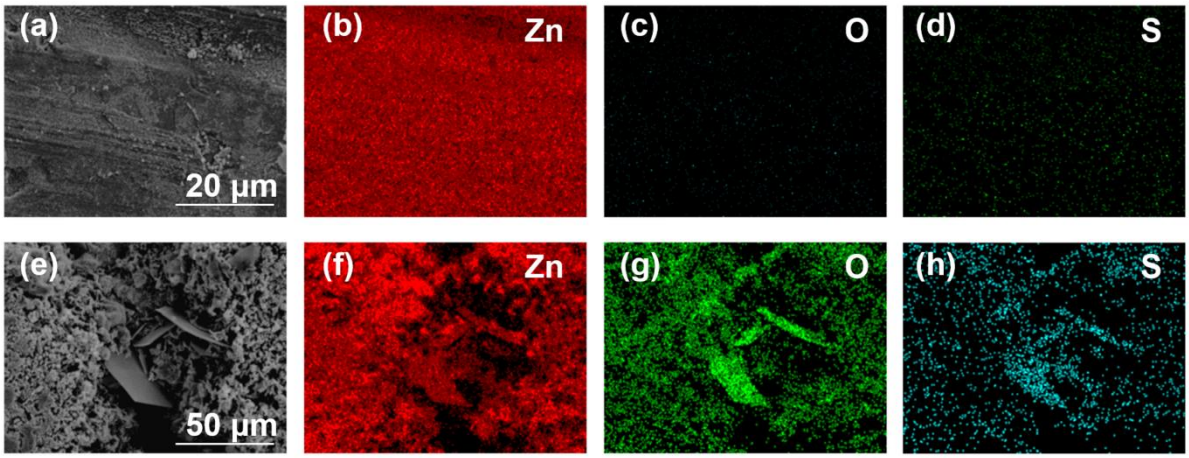

Figure S7. Surface morphology and corresponding elemental mappings of Zn electrodes after 10 mAh cm^{-2} Zn plating (1 mA cm^{-2} current density) (a-d) in $ZnSO_4$+Arg electrolyte. (e-h) in bare $ZnSO_4$ electrolyte.

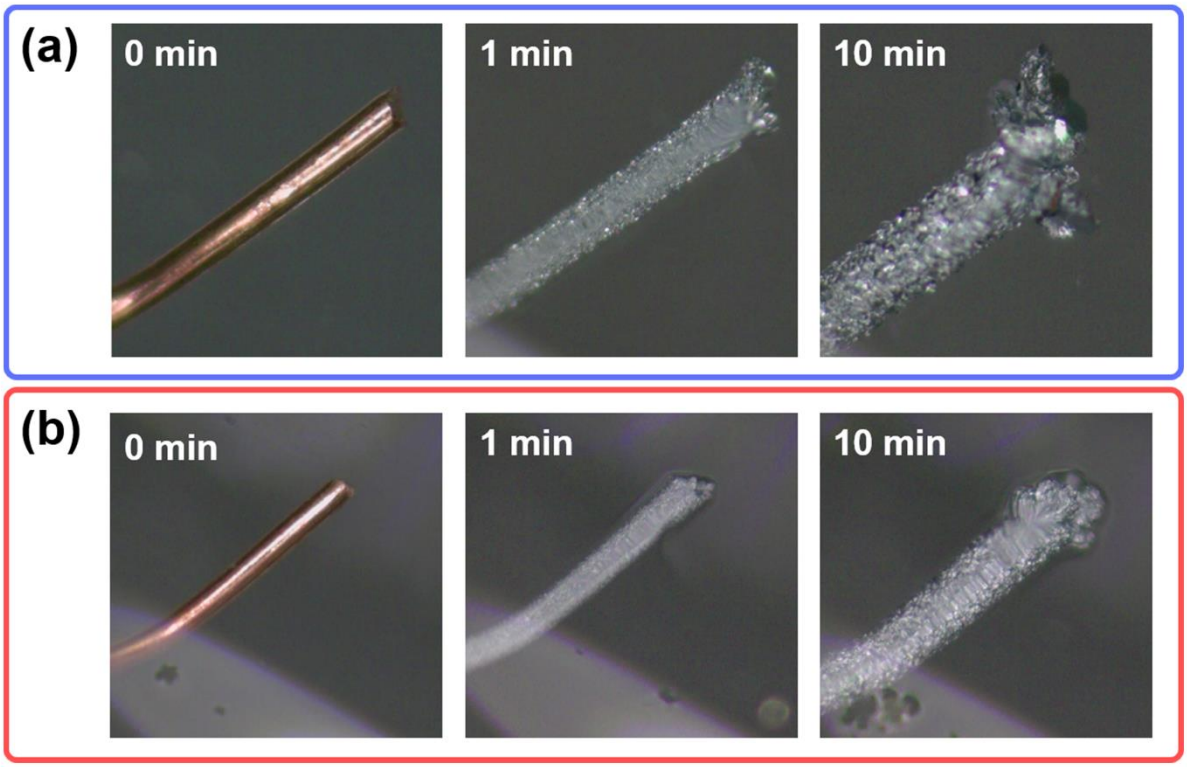

Figure S8. In-situ optical microscope image of Cu wire at 10 mA current, different Zn plating time, (a) in bare $ZnSO_4$ electrolyte and (b) in $ZnSO_4$+Arg electrolyte.

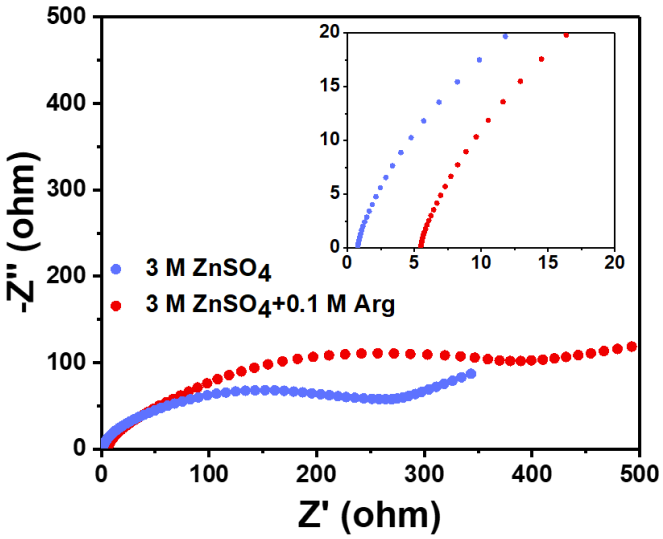

Figure S9. Nyquist plots of Zn symmetric cells in 3 M $ZnSO_4$ electrolyte and 3 M $ZnSO_4$+0.1 M Arg electrolyte, respectively.

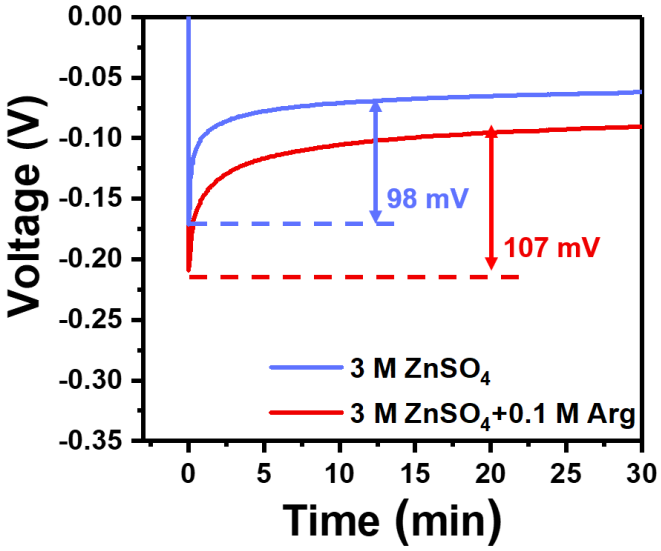

Figure S10. Nucleation overpotential of Zn symmetric cells in 3 M $ZnSO_4$ electrolyte and 3 M $ZnSO_4$+0.1 M Arg electrolyte, respectively

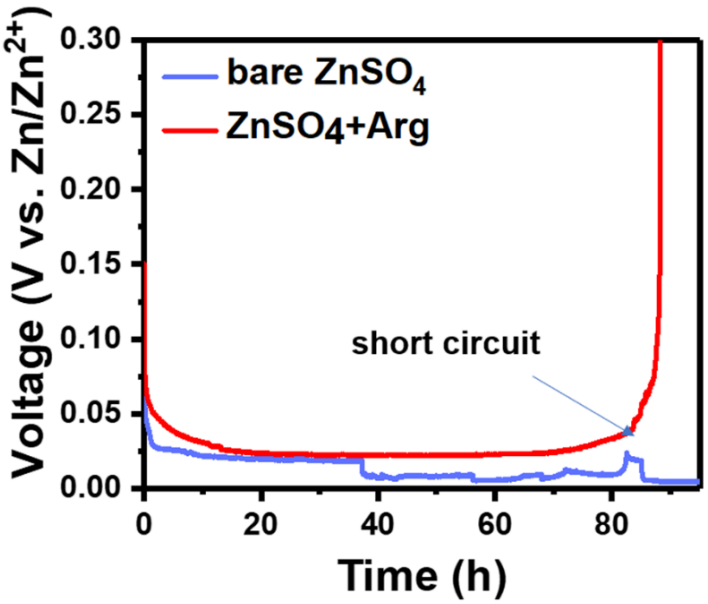

Figure S11. Symmetrical cells charge curves in bare $ZnSO_4$ and $ZnSO_4$+Arg electrolyte, current density: 1 mA cm^{-2}.

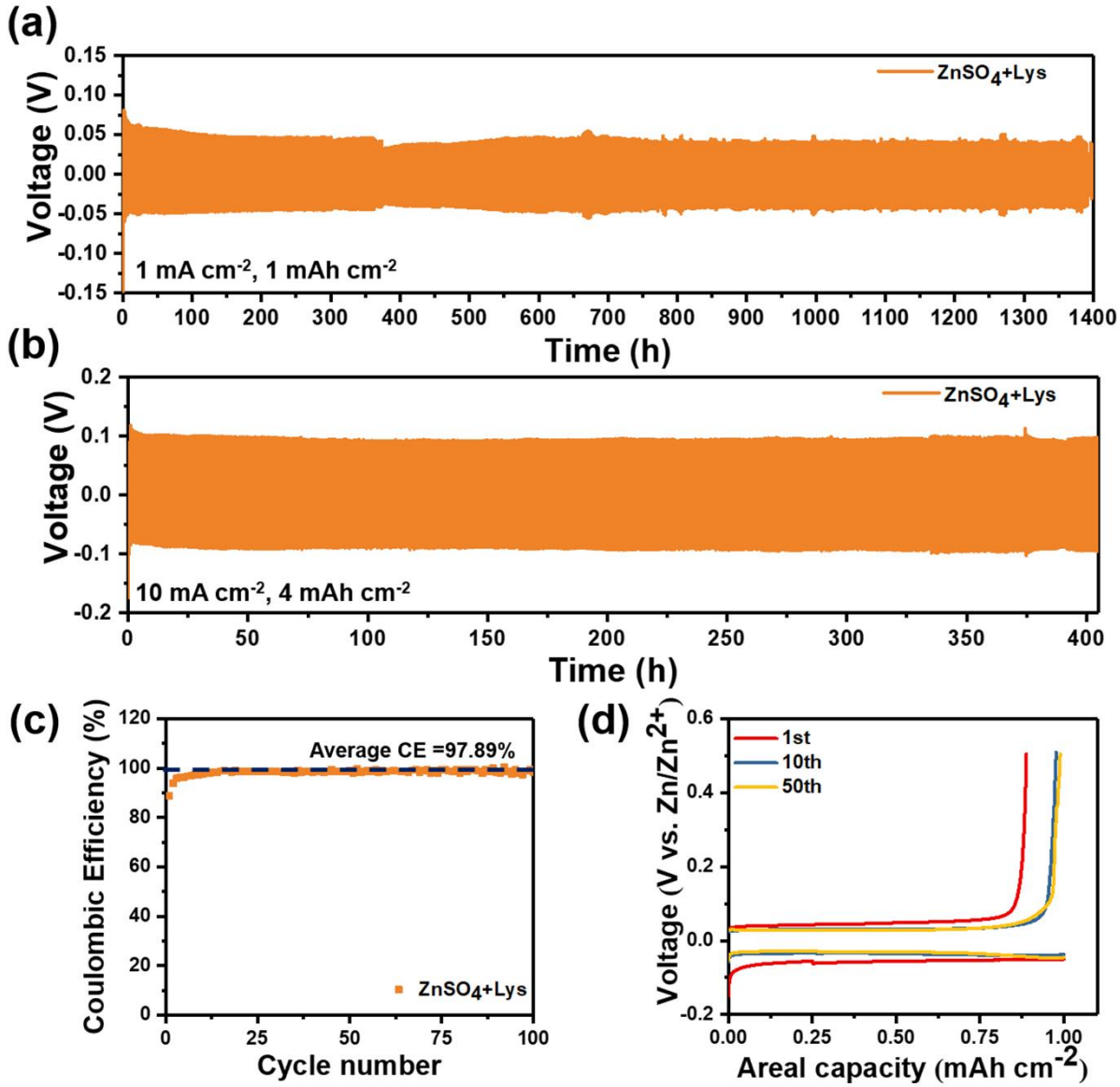

Figure S12. Galvanostatic cycling of symmetrical cell in $ZnSO_4$+Lys electrolyte at (a) 1 mA cm^{-2}, 1 mAh cm^{-2} and (b) 10 mA cm^{-2}, 4 mAh cm^{-2}. (c) CEs of Zn plating/stripping at 1 mA cm^{-2} and 1 mAh cm^{-2} and the corresponding voltage profiles (d) at different cycles.

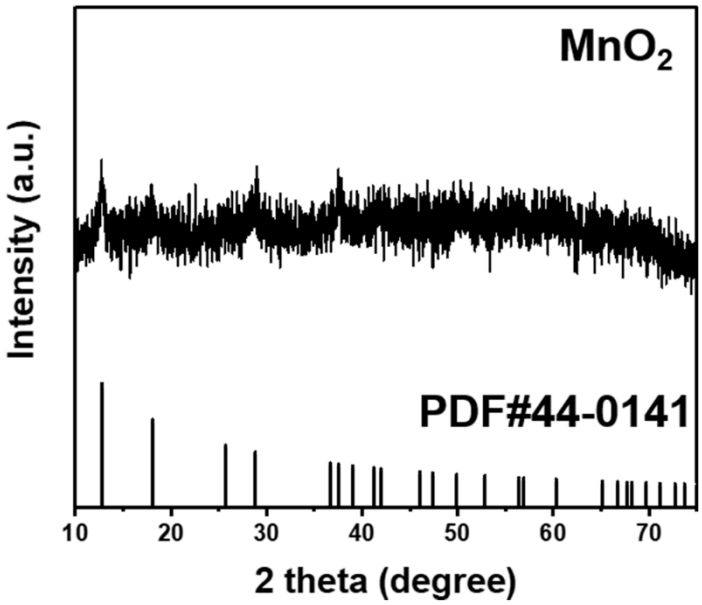

Figure S13. XRD pattern of MnO_2 showing the α-MnO_2 structure (PDF: #44-0141)

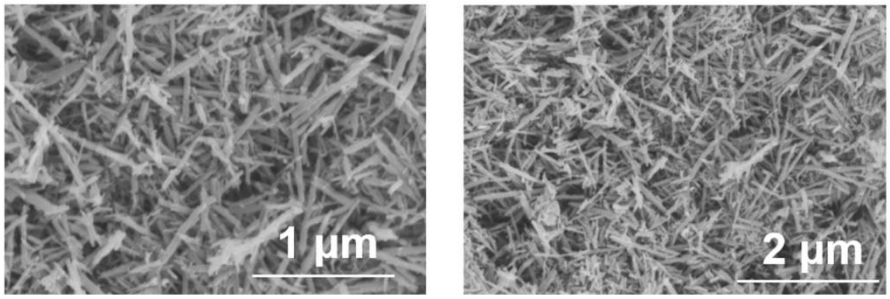

Figure S14. SEM image of MnO_2 showing the nano-rod like morphology.

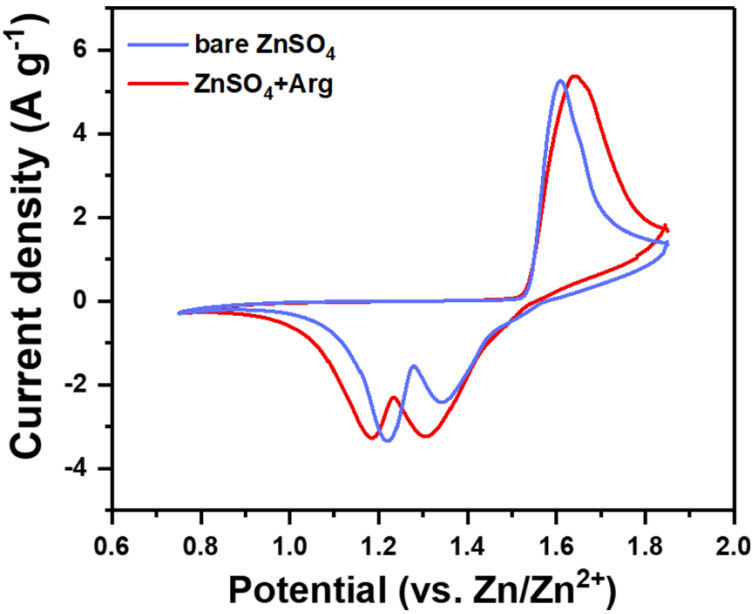

Figure S15. CV curves of MnO_2/$ZnSO_4$/Zn and MnO_2/$ZnSO_4$+Arg/Zn cells (2nd cycle, 5mV s^{-1}).

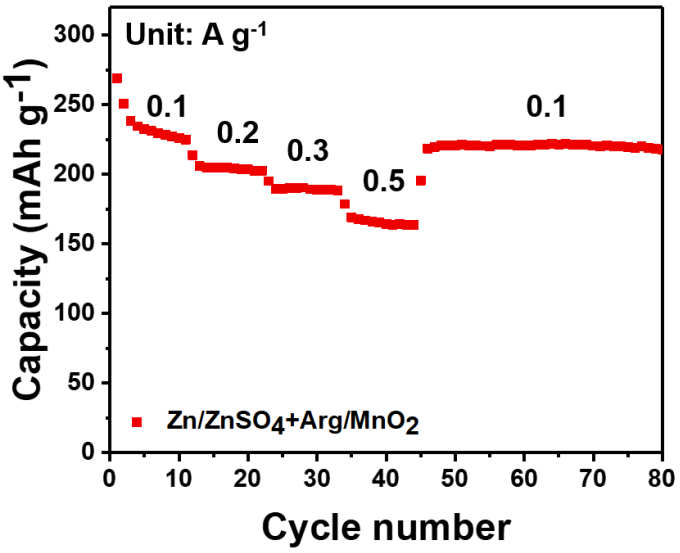

Figure S16. Rate capability of $Zn/ZnSO_4$+Arg/MnO_2 cell.

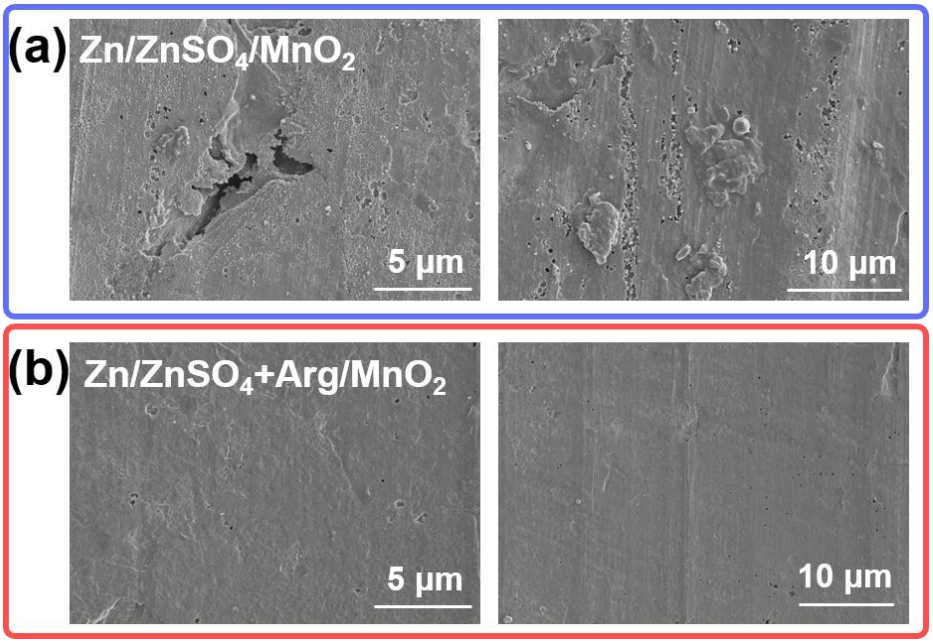

Figure S17. SEM image of Zn anode after 50 cycles in full cells: (a) $Zn/ZnSO_4/MnO_2$ cell, (b) $Zn/ZnSO_4$+Arg/MnO_2 cell.

Table S1. Ccomparison of this work with other previously reported cycling performance of symmetrical cells.

Areal capacity (mAh cm^{-2})	Current density (mA cm^{-2})	cycle life (hour)	reference
1	1	180	
4	2	280	[8]
1	20	100	
0.068	0.2	170	[9]
1	1	200	[10]
2	2	200	[11]
2.5	5	110	
1	2	140	[12]
1	1	150	[13]
5	5	160	[14]
2	10	400	
0.05	0.25	836	[1]
1	5	2100	[15]
0.125	0.25	3800	
0.5	0.5	2200	[16]
0.25	0.5	8000	[17]
10	10	150	
2	2	1100	[18]
1	1	2950	
4	5	2200	This work
4	10	900	

References

[1] L. Kang, M. Cui, F. Jiang, Y. Gao, H. Luo, J. Liu, W. Liang and C. Zhi, *Adv. Energy Mater.* **2018**, *8*, 1801090.

[2] G. Kresse and J. Furthmüller, *Comput. Mater. Sci.* **1996**, *6*, 15-50.

[3] G. Kresse and J. Furthmüller, *Phys. Rev. B* **1996**, *54*, 11169-11186.

[4] P. E. Blöchl, *Phys. Rev. B* **1994**, *50*, 17953-17979.

[5] G. Kresse and D. Joubert, *Phys. Rev. B* **1999**, *59*, 1758-1775.

[6] J. P. Perdew, K. Burke and M. Ernzerhof, Phys. Rev. Lett. **1996**, *77*, 3865-3868.

[7] S. Grimme, S. Ehrlich and L. Goerigk, *J. Comput. Chem.* **2011**, *32*, 1456-1465.

[8] Q. Zhang, J. Luan, L. Fu, S. Wu, Y. Tang, X. Ji and H. Wang, *Angew. Chem. Int. Ed.* **2019**, *58*, 15841-15847.

[9] F. Wang, O. Borodin, T. Gao, X. Fan, W. Sun, F. Han, A. Faraone, J. A. Dura, K. Xu and C. Wang, *Nat. Mater.* **2018**, *17*, 543-549.

[10] A. Naveed, H. Yang, J. Yang, Y. Nuli, J. Wang, Angew. Chem. Int. Ed. **2019**, *58*, 2760.

[11] Y. Zeng, X. Zhang, R. Qin, X. Liu, P. Fang, D. Zheng, Y. Tong and X. Lu, *Adv. Mater.* **2019**, *31*, 1903675.

[12] N. Chang, T. Li, R. Li, S. Wang, Y. Yin, H. Zhang and X. Li, *Energy Environ. Sci.* **2020***,13,* 3527-3535.

[13] K. Zhao, C. Wang, Y. Yu, M. Yan, Q. Wei, P. He, Y. Dong, Z. Zhang, X. Wang and L. Mai, *Adv. Mater. Interfaces* **2018**, *5*, 1800848.

[14] A. Bayaguud, X. Luo, Y. Fu and C. Zhu, *ACS Energy Let.* **2020**, **5**, 3012-3020.

[15] P. Liang, J. Yi, X. Liu, K. Wu, Z. Wang, J. Cui, Y. Liu, Y. Wang, Y. Xia and J. Zhang, *Adv. Funct. Mater.* **2020**, *30*, 1908528.

[16] J. Hao, X. Li, S. Zhang, F. Yang, X. Zeng, S. Zhang, G. Bo, C. Wang and Z. Guo, *Adv. Funct. Mater.* **2020**, *30*, 2001263.

[17] Z. Zhao, J. Zhao, Z. Hu, J. Li, J. Li, Y. Zhang, C. Wang and G. Cui, *Energy Environ. Sci.* **2019**, *12*, 1938-1949.

[18] J. Hao, B. Li, X. Li, X. Zeng, S. Zhang, F. Yang, S. Liu, D. Li, C. Wu and Z. Guo, *Adv. Mater.* **2020**, *32*, 2003021.